Joint Depth and Reflectivity Estimation using Single Photon LiDAR

Supplementary Material

7. Proof of Theorems

In this section, we present the proofs of the theorems. Some of the results already exist in prior literature, but in this section, we provide detailed derivations.

7.1. Proof of Theorem 1

The goal is to prove that the joint density of the number of photon detections M and the relative timestamps $\mathbf{t}_M = \{t_k\}_{k=1}^M (0 \le t_k < t_r)$ during $[0, N_r t_r)$ is

$$p\left[\mathbf{t}_M, M = m\right] = \frac{e^{-N_r\Lambda(\alpha)}}{m!} \prod_{k=1}^{m} N_r \lambda(t_k; \alpha, \tau),$$

when $M \ge 1$.

Derivation 1:

As mentioned in Sec. 3.2, M is a Poisson random variable with a mean $N_r\Lambda(\alpha)$. Thus, its probability mass function (PMF) is

$$p_M(m; \alpha) = \frac{e^{-N_r\Lambda(\alpha)} \left[N_r\Lambda(\alpha)\right]^m}{m!}, \; m = 0, 1, \dots \quad (15)$$

Conditioned on $M = m$, the m relative timestamps $\mathbf{t}_m = \{t_k\}_{k=1}^m, t_k \in [0, t_r)$ are independent and identically distributed according to the normalized photon arrival flux function as in Eq. (1), i.e.

$$f_{\tilde{t_k}|M}(t_k|m) = \frac{\lambda(t_k; \alpha, \tau)}{\Lambda(\alpha)}, \; t_k \in [0, t_r).$$

Therefore, when $M \ge 1$, the joint density is

$$\begin{aligned} p\left[\mathbf{t}_M, M = m\right] &= p_M(m) \prod_{k=1}^{m} f_{\tilde{t_k}|M}(t_k|m) \\ &= \frac{e^{-N_r\Lambda}(N_r\Lambda)^m}{m!} \prod_{k=1}^{m} \frac{\lambda(t_k)}{\Lambda} \\ &= \frac{e^{-N_r\Lambda}}{m!} \prod_{k=1}^{m} N_r \lambda(t_k). \end{aligned}$$

Additionally, when $M = 0$, the joint density reduces to the marginal PMF, i.e. $p\left[\mathbf{t}_M, M = 0\right] = p_M(0) = e^{-N_r\Lambda}$.

This derivation also appears in [6].

Derivation 2:

From the prior literature [1, 2], if we assume $\mathbf{t}_M = \{t_j\}_{j=1}^M$ such that $0 \le t_1 < t_2 < \dots < t_M < t_r$, then for $M \ge 1$,

$$p(\mathbf{t}_M, M) = e^{-N_r t_r} \prod_{j=1}^{M} N_r \lambda(t_j).$$

We identify that the statistics are ordered here. If we transform the density of ordered statistics to unordered ones as we need, the density should shrink by $m!$ due to the permutation. The desired result will then emerge.

7.2. Proof of Theorem 2

The goal is to prove

$$\left[N_r\eta^2 \int_0^{t_r} \frac{s^2(t-\tau)}{\eta\alpha s(t-\tau) + b_\lambda} \, dt\right]^{-1} \le \frac{\eta S\alpha + B}{N_r\eta^2 S^2},$$

where the equality holds if and only if $b_\lambda = 0$. Note that

$$s(t) = S \cdot \frac{1}{\sqrt{2\pi\sigma_t^2}} e^{-\frac{t^2}{2\sigma_t^2}} = S \cdot g(t),$$

where $g(t)$ is defined as the Gaussian probability density function (PDF) and we assume $g(t-\tau)$ is fully supported on the interval $[0, t_r]$, i.e. $\int_0^{t_r} g(t-\tau)\, dt = 1$. Thus, the left-hand side (LHS) becomes

$$\text{LHS} = \frac{1}{N_r\eta^2 S^2} \left[\int_0^{t_r} \frac{g^2(t-\tau)}{\eta S\alpha g(t-\tau) + b_\lambda} \, dt\right]^{-1}.$$

Then, it is equivalent to prove

$$\left[\int_0^{t_r} \frac{g^2(t-\tau)}{\eta S\alpha g(t-\tau) + b_\lambda} \, dt\right]^{-1} \le \eta S\alpha + B.$$

Starting from $\int_0^{t_r} g(t-\tau)\, dt = 1$,

$$\begin{aligned} 1 &= \int_0^{t_r} g(t-\tau)\, dt = \left[\int_0^{t_r} g(t-\tau)\, dt\right]^2 \\ &= \left[\int_0^{t_r} \underbrace{\frac{g(t-\tau)}{\sqrt{\eta S\alpha g(t-\tau) + b_\lambda}}}_{f(t)} \underbrace{\sqrt{\eta S\alpha g(t-\tau) + b_\lambda}}_{h(t)} \, dt\right]^2 \\ &\le \int_0^{t_r} \frac{g^2(t-\tau)}{\eta S\alpha g(t-\tau) + b_\lambda} \, dt \int_0^{t_r} \left[\eta S\alpha g(t-\tau) + b_\lambda\right] \, dt \\ &= \int_0^{t_r} \frac{g^2(t-\tau)}{\eta S\alpha g(t-\tau) + b_\lambda} \, dt \cdot (\eta S\alpha + B), \end{aligned}$$

where the Cauchy-Schwarz inequality is applied from the second line to the third, and the equality holds if and only if $h(t) = k \cdot f(t)$ for $k \ne 0$, or equivalently $b_\lambda = 0$.

Rearrange the terms at the last line, we obtain

$$\left[\int_0^{t_r} \frac{g^2(t-\tau)}{\eta S\alpha g(t-\tau) + b_\lambda} \, dt\right]^{-1} \le \eta S\alpha + B,$$

and the proof is complete.

This is a **new** derivation we make for this paper.

8. Proof of Additional Results

We provide the detailed derivations of equations and corollaries in Sec. 3, some of which have already appeared in previous papers.

8.1. Joint MLE in Eq. 3

This is the joint MLE, where we provide detailed steps to derive the objective function.

$$\begin{aligned}(\widehat{\tau},\widehat{\alpha}) &= \underset{0<\tau<t_r,\alpha\geq 0}{\text{argmax}} \; p\left[\mathbf{t}_M, M=m\right] \\ &= \underset{0<\tau<t_r,\alpha\geq 0}{\text{argmax}} \; \log\, p\left[\mathbf{t}_M, M=m\right] \\ &= \underset{0<\tau<t_r,\alpha\geq 0}{\text{argmax}} \Big\{ -N_r(\eta S\alpha + B) - \log(m!) \\ &\qquad + m\log(N_r) + \sum_{k=1}^{m}\log\lambda(t_k)\Big\} \\ &= \underset{0<\tau<t_r,\alpha\geq 0}{\text{argmax}} \Big\{ -N_r\eta S\alpha \\ &\qquad + \sum_{k=1}^{m}\log\left(\eta\alpha s\left(t_k-\tau\right)+b_\lambda\right)\Big\},\end{aligned}$$

where irrelevant terms are dropped from the third line to the fourth one.

8.2. Proof of Corollary 1

These are the individual ML estimators for depth and reflectivity estimation.

Derivation of Eq. (4):

Assume $b_\lambda = 0$ and τ is a known constant. Then, becomes Eq. (3)

$$\begin{aligned}\widehat{\alpha} &= \underset{\alpha\geq 0}{\text{argmax}} \Big\{ -N_r\eta S\alpha + \sum_{k=1}^{m}\log\left(\eta\alpha s\left(t_k-\tau\right)\right)\Big\} \\ &= \underset{\alpha\geq 0}{\text{argmax}} \Big\{ m\log\alpha + \sum_{k=1}^{m}\log\left(\eta s\left(t_k-\tau\right)\right) - N_r\eta S\alpha\Big\} \\ &= \underset{\alpha\geq 0}{\text{argmax}} \underbrace{\Big\{ m\log\alpha - N_r\eta S\alpha\Big\}}_{L(\alpha)},\end{aligned}$$

where terms irrelevant to α are eliminated from the second to third line.

To solve $\widehat{\alpha}$,

$$\frac{dL(\alpha)}{d\alpha} = \frac{m}{\alpha} - N_r\eta S = 0,$$

and thus $\widehat{\alpha} = m/N_r\eta S$. We examine that the $\alpha \geq 0$ constraint is intrinsically satisfied.

Derivation of Eq. (5):

Assume $b_\lambda = 0$ and α is a known constant. Then, Eq. (3) becomes

$$\begin{aligned}\widehat{\tau} &= \underset{0<\tau<t_r}{\text{argmax}} \Big\{ -N_r\eta S\alpha + \sum_{k=1}^{m}\log\left(\eta\alpha s\left(t_k-\tau\right)\right)\Big\} \\ &= \underset{0<\tau<t_r}{\text{argmax}} \Big\{ \sum_{k=1}^{m}\log\left[s\left(t_k-\tau\right)\right] - N_r\eta S\alpha + m\log(\eta\alpha)\Big\} \\ &= \underset{0<\tau<t_r}{\text{argmax}} \underbrace{\Big\{ \sum_{k=1}^{m}\log\left[s\left(t_k-\tau\right)\right]\Big\}}_{L(\tau)},\end{aligned}$$

where parameters irrelevant to τ are removed from the second to third line and $s(\cdot)$ is a Gaussian-shaped function.

To solve $\widehat{\tau}$,

$$\frac{dL(\tau)}{d\tau} = \sum_{k=1}^{m}\frac{s\left(t_k-\tau\right)\cdot\left[(t_k-\tau)/\sigma_t^2\right]}{s\left(t_k-\tau\right)} = 0,$$

which is equivalent to solve

$$\frac{dL(\tau)}{d\tau} = \sum_{k=1}^{m}(t_k-\tau) = \sum_{k=1}^{m}t_k - m\tau = 0,$$

and thus $\widehat{\tau} = \frac{1}{m}\sum_{k=1}^{m}t_k$. We examine that the $0<\tau<t_r$ constraint is intrinsically satisfied.

8.3. Reflectivity estimator w/o depth in Eq. (6)

First, we can derive an **unconstrained** MLE from Eq. (15). The log-likelihood is

$$\log\; p_M(m;\alpha) = -N_r\Lambda(\alpha) + m\log(N_r\Lambda(\alpha)) - \log(m!).$$

To maximize the log-likelihood function, it is necessary that

$$\frac{\partial\log\; p_M(m;\alpha)}{\partial\alpha} = -N_r\eta S + \frac{m\eta S}{\eta S\alpha + B} = 0. \tag{16}$$

Solve the equation above, the **unconstrained** MLE is

$$\widehat{\alpha}_{\text{c}}^{*} = \frac{1}{\eta S}\left(\frac{m}{N_r} - B\right).$$

Accordingly, the **constrained** MLE for the reflectivity without the help of depth is

$$\widehat{\alpha}_{\text{c}} = \max\left\{\widehat{\alpha}_{\text{c}}^{*},\, 0\right\}.$$

8.4. Proof of Corollary 2

Although it is unlikely to derive the CRLB for the biased CML estimator $\widehat{\alpha}_{\text{c}}$ [9], we can analyze the CRLB for $\widehat{\alpha}_{\text{c}}^{*}$ to gain some insight on the performance of $\widehat{\alpha}_{\text{c}}$.

Based on Eq. (16), the second derivative is

$$\frac{\partial^2\log\; p_M(m;\alpha)}{\partial\alpha^2} = -\frac{m\eta^2S^2}{(\eta S\alpha + B)^2}.$$

The Fisher information is

$$I(\alpha) = -\mathbb{E}\left[\frac{\partial^2 \log\ p_M(m;\alpha)}{\partial \alpha^2}\right] = \frac{\eta^2 S^2}{(\eta S\alpha + B)^2}\mathbb{E}[m]$$
$$= \frac{\eta^2 S^2}{(\eta S\alpha + B)^2} N_r(\eta S\alpha + B)$$
$$= \frac{N_r \eta^2 S^2}{\eta S\alpha + B}.$$

Thus, the CRLB is

$$\text{Var}\left[\widehat{\alpha}_{\text{c}}^*\right] \geq \frac{1}{I(\alpha)} = \frac{\eta S\alpha + B}{N_r \eta^2 S^2} = \frac{1 + 1/SBR}{N_r(\eta S/\alpha)}.$$

To the best of our knowledge, though the result is consistent with the limiting CRLB of a Binomial photon count estimator reported in [9], the CRLB derivation for this Poisson photon count reflectivity estimator may be new.

8.5. Reflectivity estimator w/ depth in Eq. (8)

Assume τ is a known constant. Then, Eq. (3) turns to

$$\widehat{\alpha} = \underset{\alpha \geq 0}{\text{argmax}} \underbrace{\left\{ -N_r \eta S\alpha + \sum_{k=1}^{m} \log\left(\eta \alpha s\left(t_k - \tau\right) + b_\lambda\right) \right\}}_{L_t(\alpha)}.$$

To solve the **unconstrained** MLE $\widehat{\alpha}_{\text{t}}^*$, it is necessary that

$$\frac{dL_t(\alpha)}{d\alpha} = -N_r \eta S + \sum_{k=1}^{m} \frac{\eta s\left(t_k - \tau\right)}{\eta \alpha s\left(t_k - \tau\right) + b_\lambda} = 0. \quad (17)$$

Rearrange the terms, and then Eq. (3) will appear. The result is consistent with [7].

Discussion. It is stated in [7] that the left-hand side of Eq. (3) is monotonically decreasing in α, so a unique optical estimate of α exists. However, we notify that Eq. (3) has m negative roots. More rigorously speaking, the LHS is monotonically decreasing within $[0, \infty)$ which is of interest in the CML estimation. As a result, we design a simple and robust algorithm to numerically compute the solution, as shown in Sec. 9.3. But theoretically, the CML estimator with the help of depth is given by

$$\widehat{\alpha}_t = \max\left\{\widehat{\alpha}_t^*, 0\right\}.$$

8.6. Proof of Corollary 3

Similar to Sec. 8.4, we derive the CRLB for the **unconstrained** MLE $\widehat{\alpha}_t^*$ in order to have a sense of how the CML estimator $\widehat{\alpha}_t$ will behave.

We point out that the first derivative of the log-likelihood of the joint density

$$\frac{\partial \log p\left[\mathbf{t}_M, M = m; \alpha\right]}{\partial \alpha} = \frac{dL_t(\alpha)}{d\alpha},$$

where the right-hand side is shown in Eq. (17).

Building on this, the second derivative is

$$\frac{\partial^2 \log p}{\partial \alpha^2} = -\sum_{k=1}^{m} \frac{\eta^2 s^2\left(t_k - \tau\right)}{\left(\eta \alpha s\left(t_k - \tau\right) + b_\lambda\right)^2}.$$

The Fisher information is

$$I(\alpha) = -\mathbb{E}\left[\frac{\partial^2 \log p}{\partial \alpha^2}\right] = \mathbb{E}\left[\sum_{k=1}^{m} \frac{\eta^2 s^2\left(t_k - \tau\right)}{\left(\eta \alpha s\left(t_k - \tau\right) + b_\lambda\right)^2}\right]$$
$$= N_r \Lambda \mathbb{E}\left[\frac{\eta^2 s^2\left(t - \tau\right)}{\left(\eta \alpha s\left(t - \tau\right) + b_\lambda\right)^2}\right]$$
$$= N_r \Lambda \int_{-\infty}^{\infty} \frac{\eta^2 s^2\left(t - \tau\right)}{\left(\eta \alpha s\left(t - \tau\right) + b_\lambda\right)^2} \frac{\eta \alpha s\left(t - \tau\right) + b_\lambda}{\Lambda}\, dt$$
$$= N_r \eta^2 \int_0^{t_r} \frac{s^2\left(t - \tau\right)}{\eta \alpha s\left(t - \tau\right) + b_\lambda}\, dt,$$

where the derivation from the first to the second line will be shown below.

Define $g(t) = \frac{\eta^2 s^2(t-\tau)}{(\eta \alpha s(t-\tau) + b_\lambda)^2}$.

$$\mathbb{E}\left[\sum_{k=1}^{m} \frac{\eta^2 s^2\left(t_k - \tau\right)}{\left(\eta \alpha s\left(t_k - \tau\right) + b_\lambda\right)^2}\right] = \mathbb{E}\left[\sum_{k=1}^{m} g(t_k)\right]$$
$$= \sum_{m=0}^{\infty} \underbrace{\int_0^{t_r} \cdots \int_0^{t_r}}_{m} \sum_{k=1}^{m} g(t_k) p\left[\mathbf{t}_M, M = m\right]\, dt_1 \ldots dt_m$$
$$= \sum_{m=0}^{\infty} \underbrace{\int_0^{t_r} \cdots \int_0^{t_r}}_{m} \sum_{k=1}^{m} g(t_k) p_M(m)$$
$$\prod_{k=1}^{m} f_{\tilde{t_k}|M}(t_k|m)\, dt_1 \ldots dt_m$$
$$= \sum_{m=0}^{\infty} p_M(m) \underbrace{\int_0^{t_r} \cdots \int_0^{t_r}}_{m} \left[g(t_1) + \sum_{k=2}^{m} g(t_k)\right]$$
$$f_{\tilde{t_1}|M}(t_1|m)\, dt_1 \ldots f_{\tilde{t_m}|M}(t_m|m)\, dt_m$$
$$= \sum_{m=0}^{\infty} p_M(m) \underbrace{\int_0^{t_r} \cdots \int_0^{t_r}}_{m-1} \left[\mathbb{E}[g(t_1)] + \sum_{k=2}^{m} g(t_k)\right]$$
$$f_{\tilde{t_2}|M}(t_2|m)\, dt_2 \ldots f_{\tilde{t_m}|M}(t_m|m)\, dt_m$$
$$= \sum_{m=0}^{\infty} p_M(m) \sum_{k=1}^{m} \mathbb{E}[g(t_k)] = \sum_{m=0}^{\infty} p_M(m) \sum_{k=1}^{m} \mathbb{E}[g(t)]$$
$$= \mathbb{E}[g(t)] \sum_{m=0}^{\infty} m p_M(m) = \mathbb{E}[g(t)]\mathbb{E}[M]$$
$$= N_r \Lambda \mathbb{E}\left[g(t)\right] = N_r \Lambda \mathbb{E}\left[\frac{\eta^2 s^2\left(t - \tau\right)}{\left(\eta \alpha s\left(t - \tau\right) + b_\lambda\right)^2}\right].$$

Thus, the CRLB is

$$\mathrm{Var}\left[\widehat{\alpha}_{\mathrm{t}}^{*}\right] \geq \frac{1}{I(\alpha)} = \left[N_r \eta^2 \int_0^{t_r} \frac{s^2(t-\tau)}{\eta\alpha s(t-\tau)+b_\lambda}\, dt\right]^{-1}.$$

Although the CRLB analysis of $\widehat{\alpha}_t^*$ is presented in [6], here we provide the explicit formula for the first time.

9. Numerical Verification of Information Sharing under MLE

Although how reflectivity helps depth is obvious and we have the CRLB analysis to support the reverse direction, one may argue that the CRLB is for the unconstrained MLE rather than the true CML estimation. To fix this concern, we conduct a numerical simulation to further verify the mutual benefit between depth and reflectivity.

9.1. Simulation and experimental setups

We simulate timestamps for one pixel using the Poisson photon arrival statistics under a low photon level and different SBRs. Due to the randomness, we repeat the experiment multiple times. The simulation specifications are summarized in Tab. 4.

Symbols	Meaning	Values
t_r	repetition period	10
N_r	# repetition	1000
τ	ground truth time delay	4
α	ground truth reflectivity	0.5
t	temporal duration	$0 \leq t < 10$
dt	temporal resolution	$1/1000$
σ_t	pulse width	0.2
$N_r\Lambda$	average photon level	10
SBR	signal-to-background ratio	$\{0.5, 1, 2, 5, 10\}$
`iter_num`	# repetitive experiments	$\{1000, 50\}$

Table 4. Simulation specifications. $\{\cdot\}$ means a list of values used.

Then, we numerically solve the depth and reflectivity estimation with and without the help of one another, respectively. In the case where they are independent, both estimations are easily tractable because of the close-form equations in Eqs. (5) and (6).

However, when they rely on each other, no close-form solution is available. Therefore, a search-based algorithm is required. We demonstrate the difficulty of the two optimization problems and propose corresponding solutions to them in the next two subsections, respectively.

Finally, the MSE results validate the information sharing, as can be seen in Fig. 2. Here, we choose `iter_num` $=$ 1000.

9.2. Depth estimation and a search algorithm

Assume α is a known constant. Then, Eq. (3) turns to

$$\widehat{\tau} = \underset{0<\tau<t_r}{\operatorname{argmax}} \underbrace{\left\{\sum_{k=1}^{m} \log\left(\eta\alpha s\left(t_k-\tau\right)+b_\lambda\right)\right\}}_{L_d(\tau)}.$$

To solve the unconstrained MLE $\widehat{\tau}_{\mathrm{t}}^{*}$, it is necessary that

$$\frac{dL_d(\tau)}{d\tau} = \frac{\eta\alpha\dot{s}\left(t_k-\tau\right)}{\eta\alpha s\left(t_k-\tau\right)+b_\lambda} = 0.$$

Nevertheless, even if the constraint that $0 < \tau < t_r$ is forced, an ordinary numerical solver may be trapped in a local minima, especially when the SBR is low. To visualize this, we plot two typical realizations of $\frac{d}{d\tau}L_d(\tau)$ in Fig. 13.

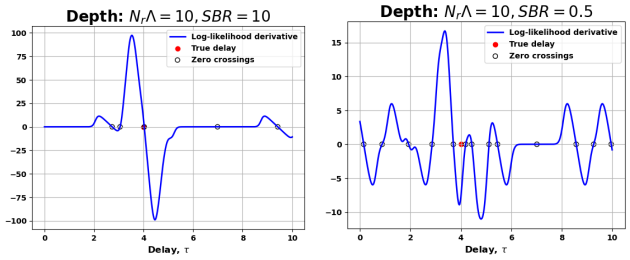

(a) (b)

Figure 13. Visualization of $\frac{d}{d\tau}L_d(\tau)$. (a). The number of local minima is acceptable when the SBR is high. (b). Low SBR incurs much more local minima near the ground truth.

As shown in Fig. 13b, since a number of zero crossings exist near the ground truth, although we start at the ground truth, there is no guarantee for the solver to converge to the true value. Thus, we gradually search for the local minima closest to the ground truth to robustly solve the optimization, as summarized in Algorithm 1.

Depth estimation results. In addition to the MSE plot from the main text, we provide the scatter plot of `iter_num` $=$ 50 experiments to visualize the estimation performance with and without knowledge of reflectivity, in Fig. 14.

From the figure, with the reflectivity information, the variance of the depth estimation is much smaller, proving a better recovery.

9.3. Reflectivity estimation and a robust algorithm

To solve the reflectivity estimation with the help of depth, Eq. (17) is required. Likewise, this optimization problem also suffers from local minima. We plot $\frac{d}{d\alpha}L_t(\alpha)$ in Fig. 15.

The local minimum problem in the reflectivity estimation is more severe because they cluster so close together. We can design a search-based algorithm similar to Algorithm 1. However, it is typically slow and inaccurate.

Algorithm 1 Robust Depth Estimation Algorithm

Require: Initial guess τ_0, step size `step`, maximum iterations $N_{\max}$, iteration number `iter`
Ensure: Estimated depth $\hat{\tau}$
Initialize $\hat{\tau} \leftarrow \tau_0$, $a \leftarrow \tau_0$, $b \leftarrow \tau_0$, `iter` $\leftarrow 1$
Define $dL_d(\tau)$ ▷ Derivative of likelihood function
while sign$[dL_d(a)]$ = sign$[dL_d(b)]$ **and** `iter` $< N_{\max}$ **do**
    $a \leftarrow a -$ `step`
    $b \leftarrow b +$ `step`
end while
if sign$[dL_d(a)] \neq$ sign$[dL_d(b)]$ **then**
    Solve $\hat{\tau}$ such that $dL_d(\hat{\tau}) = 0$ using a root-finding method on $[a, b]$
else
    Return *Error: "Bracket not found"*
end if
Return $\hat{\tau}$

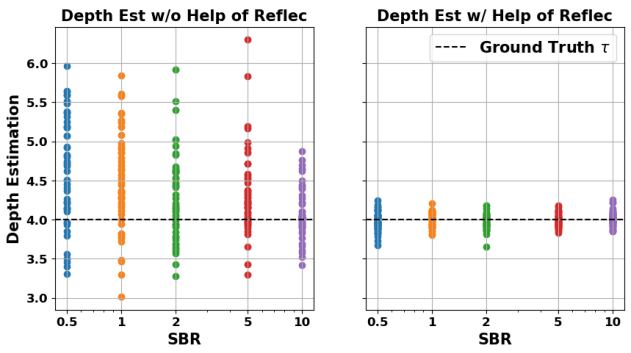

Figure 14. Depth estimation with and without the help of reflectivity.

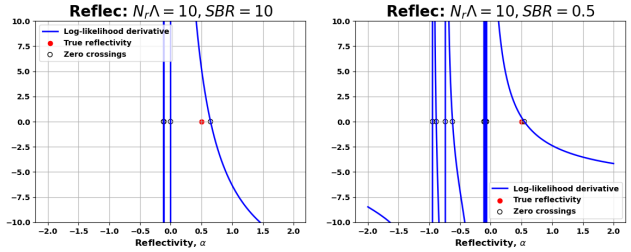

(a) (b)

Figure 15. Visualization of $\frac{d}{d\alpha}L_t(\alpha)$. (a). High SBR. (b). Low SBR causes more local minima.

We recognize that the function is monotonically decreasing within $[0, \infty)$, and the optimization is also constrained on this region. Therefore, we propose an algorithm based on `bisect` for the reflectivity estimation, as illustrated in Algorithm 2.

Reflectivity estimation results. Using the Algorithm 2,

Algorithm 2 Robust Reflectivity Estimation Algorithm

Ensure: Estimated reflectivity $\hat{\alpha}$
Initialize b as a large positive value
Define $dL_t(\alpha)$ ▷ Derivative of likelihood function
if $dL_t(0) \leq 0$ **then**
    $\hat{\alpha} \leftarrow 0$
else
    Solve $\hat{\alpha}$ such that $dL_t(\hat{\alpha}) = 0$ using the bisect method on the interval $(0, b)$
end if
Return $\hat{\alpha}$

we draw the scatter plot to evaluate the reflectivity estimation performance with and without knowledge of depth in Fig. 16.

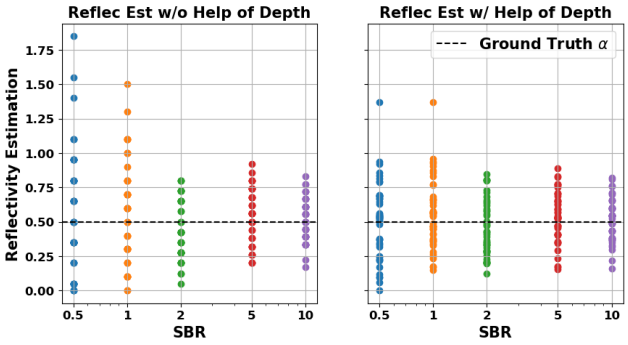

Figure 16. Reflectivity estimation with and without the help of depth.

From the figure, the reflectivity estimation is much better with the help of depth, resulting in fewer 0 estimates particularly when the SBR is low.

10. Simulation Pipeline

In this section, we provide a detailed description of how the SP-LiDAR simulation is conducted. The arrangement of a typical SP-LiDAR setup is illustrated in Fig. 17. As outlined in the main text, we adopt the most reasonable SP-LiDAR parameter settings, assuming no multi-path interactions, pulse elongation, crosstalk, or dead time. Under these assumptions, we can presume the independence of the captured photons.

Furthermore, the scene is quasi-static, meaning it remains stationary during each exposure time. This is a reasonable assumption, considering the laser source operates in the MHz range. We replicate the operation of the SPAD sensor described in [4], which is capable of registering the first photon during each reading cycle, following the first-photon behavior as depicted in Fig. 18.

Given that there is at least one photon registration, i.e.,

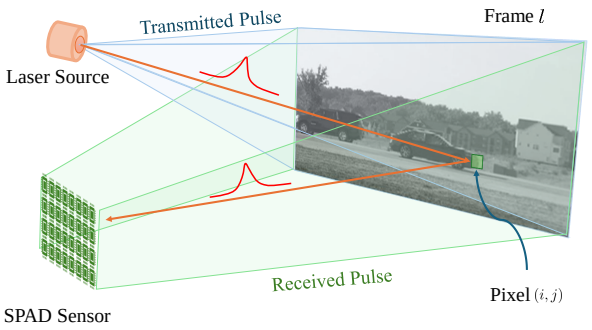

Figure 17. The SPL imaging setup showcases the main components of the arrangement. The laser source emits pulses in rapid succession, whereas the SPAD sensor records the time of arrival of photons.

the outcome from Eq. (15) is $M > 0$, the timestamp distribution of the first photon detected of each pixel (i, j) can be modeled as a mixture distribution as follows:

$$p[t] = \frac{\eta\alpha_{i,j}S}{\eta\alpha_{i,j}S + B_{i,j}} \left(\frac{s\left(t_{i,j} - \frac{2z_{i,j}}{c} - t_{\text{jit}}\right)}{S} \right) + \frac{B_{i,j}}{\eta\alpha_{i,j}S + B_{i,j}} \left(\frac{1}{t_r}\right), \tag{18}$$

Where $t_{\text{jit}} \sim \mathcal{N}(0, \sigma_j)$ is the timing jitter, a temporal error interval, caused by the temporal response of the SPAD setup. Without loss of generality, we assume that the laser pulse $s(t)$ is a Gaussian pulse $\mathcal{N}(0, \sigma_t)$, yielding $S = \int_{-t_r/2}^{t_r/2} s(t), dt = 1$. Therefore, the distribution can be further simplified to:

$$p[t] = \frac{\eta\alpha_{i,j}}{\eta\alpha_{i,j} + B_{i,j}} \left(s\left(t_{i,j} - \frac{2z_{i,j}}{c} - t_{\text{jit}}\right)\right) + \frac{B_{i,j}}{\eta\alpha_{i,j} + B_{i,j}} \left(\frac{1}{t_r}\right). \tag{19}$$

To calculate the reflectivity of each pixel $\alpha_{i,j}$, i.e., the average number of photons per pixel, we use:

$$\alpha_{i,j} = \frac{E_0}{hc/\lambda} \cdot \frac{10^{-\alpha_{\text{atm}} \cdot 2R}\, \Gamma_{i,j}}{8 f_{\text{no}}^2} \cdot \frac{W_p H_p}{A_{\text{illum}}}, \tag{20}$$

and the average number of photons from the background $B_{i,j}^{\text{bck}}$ and the dark current B^{dc} are modeled, respectively, as:

$$B_{i,j}^{\text{bck}} = \frac{W^{\text{bck}}}{hc/\lambda} \cdot \frac{10^{-\alpha_{\text{atm}} \cdot R}\, \Gamma_{i,j}}{8 f_{\text{no}}^2} \cdot \frac{W_p H_p}{A_{\text{illum}}} \cdot t_r, \tag{21}$$

$$B^{\text{dc}} = C^{\text{dc}} t_r. \tag{22}$$

Where $B_{i,j} = \eta B_{i,j}^{\text{bck}} + B^{\text{dc}}$, and A_{illum} indicates the area of illumination by the source. The above equations inherently follow the models introduced in [8]. All the notations and the corresponding parameter values used for this simulation are listed in Tab. 5.

To obtain high-speed depth maps, we utilized an RGB 2000-FPS video dataset [3], which was subsequently processed using the monocular depth estimation algorithm *Depth Anything V2* [10] to generate ground truth depth maps. Using pre-trained models, we could only acquire relative depth variations. Therefore, these depth map values were converted into absolute depth map values, denoted as $z_{i,j}$. For reflectance $\Gamma_{i,j}$, we used the grayscale values of RGB images, a common practice in SP-LiDAR literature. Once all parameters were obtained, we sample timestamps from the PDF provided in Eq. (19) based on the outcomes of a Bernoulli distribution with specified probabilities.

$$\mathrm{P}_{i,j}^{\text{sig}} = \frac{\eta\alpha_{i,j}}{\eta\alpha_{i,j} + B_{i,j}} \tag{23}$$

$$\mathrm{P}_{i,j}^{\text{noise}} = \frac{B_{i,j}}{\eta\alpha_{i,j} + B_{i,j}} \tag{24}$$

Where $\mathrm{P}_{i,j}^{\text{sig}}$ denotes the probability that the detected photon originates from the signal, and $\mathrm{P}_{i,j}^{\text{noise}}$ represents the probability of the detected photon originating from noise. If the outcome of the Bernoulli trial is signal, the timestamp is sampled from the corresponding shifted version of the signal $s(t)$. Otherwise, the timestamp is sampled from the uniform distribution $\mathcal{U}(0, t_r)$. The sampling mechanism is applied to all the pixels in each frame across all frames in each video. The overall simulation process is illustrated in Fig. 19.

11. Visualization of Common Features

This section explains the visualization of the common features from the experiment conducted in Sec (3.3), focusing on the latent space of both reflectivity and depth. The input images for depth and reflectivity have a size of $128\times128\times1$, and the feature map size is gradually reduced to produce a latent feature map of $8 \times 8 \times 128$, achieving a compression ratio of $2\times$ for each branch. One-third of the latent feature map, i.e., a feature map of size $8\times8\times43$, is trained to extract the common features shared by both depth and reflectivity.

To visualize these common features in a low-dimensional space, we use Principal Component Analysis (PCA). PCA is a dimensionality reduction technique that linearly transforms the data into a new coordinate system, making it easier to identify the directions — also known as principal components (PCs) — that capture the most significant variations [5]. Using PCA, the original 128×43 common feature map $\mathcal{H}_{\text{lsFeat}} = [\mathcal{R}_{\text{lsFeat}}, \mathcal{D}_{\text{lsFeat}}]$ are projected into a 128×3 low-dimensional feature space. Mathematically, the projection is formulated as

$$\mathcal{H}_{\text{lsFeat}}^{\text{pca}} = \mathcal{H}_{\text{lsFeat}}^{c} W, \tag{25}$$

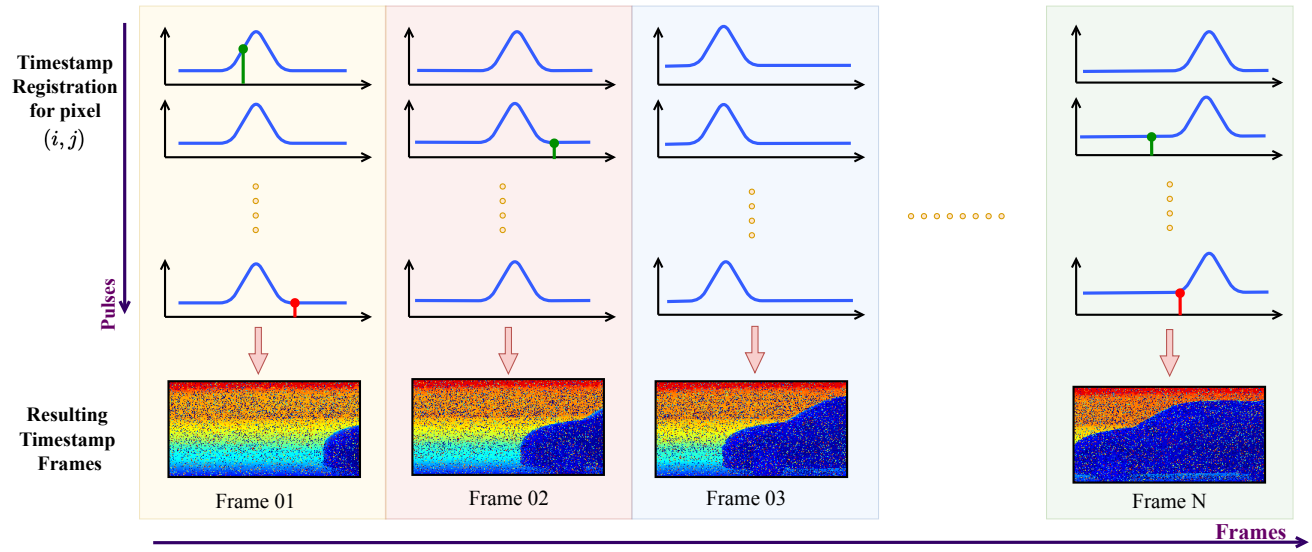

Figure 18. The timestamp registration of the SPAD sensor demonstrates the behavior of the first photon for each pixel (i, j). During the exposure time $t_{\text{exp}} = N_r t_r$, only the first photon is detected. Successful registrations are marked in green, while missed photons are marked in red. Timestamps are recorded for all pixels, resulting in the generation of timestamp frames.

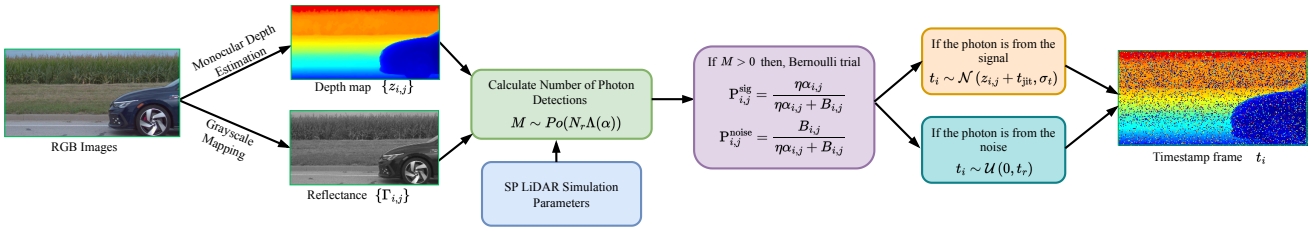

Figure 19. Overview of the SPL simulation process demonstrates the key components of the pipeline.

where $W = [v_1\ v_2 \cdots v_k] \in \mathbb{R}^{p \times k}$ is the projection matrix, constructed from the eigenvectors corresponding to the largest k eigenvalues of the covariance matrix of $\mathcal{H}^{c}_{\text{lsFeat}} \in \mathbb{R}^{n \times p}$, the centered latent feature maps. Here, $p = 43$ and $n = 128$ denote the number of features and the number of samples, respectively, while $k = 3$ represents the number of PCs. The resulting transformed feature map is $\mathcal{H}^{\text{pca}}_{\text{lsFeat}} \in \mathbb{R}^{n \times k}$. Similarly, to showcase other latent features of depth and reflectivity, the same procedure is followed. Fig. 20 illustrates how the common features and other features are distributed in the low-dimensional space.

Parameter	Symbol	Value
Dark counts	C^{dc}	126 Hz
Plank constant	h	6.626×10^{-34} m^{2}kgs^{-1}
Wavelength	λ	671 nm
Attenuation coefficient	α_{atm}	0.7dB km^{-1}
f-number	f_{no}	2.0
Reflectance	$\Gamma_{i,j}$	[0.0, 1.0]
Height of an effective pixel	H_p	9.2 μm
Width of an effective pixel	W_p	9.2 μm
Exposure time	t_{exp}	1000 μs
Jitter variation	σ_j	220 ps
Range	R	30 m
Pulse width	σ_t	1 ns
Energy per pulse	E_0	1.219 nJ
Background radiation	W^{bck}	0 W
Background radiation for Ablation	W^{bck}	0.0004 W
Repetition rate	$1/t_r$	2.25 MHz
Depth variation	$z_{i,j}$	[2 m, 60 m]
Efficiency of the sensor	η	0.18
Speed of Light	c	3×10^8ms^{-1}

Table 5. SP-LiDAR Simulation Parameters

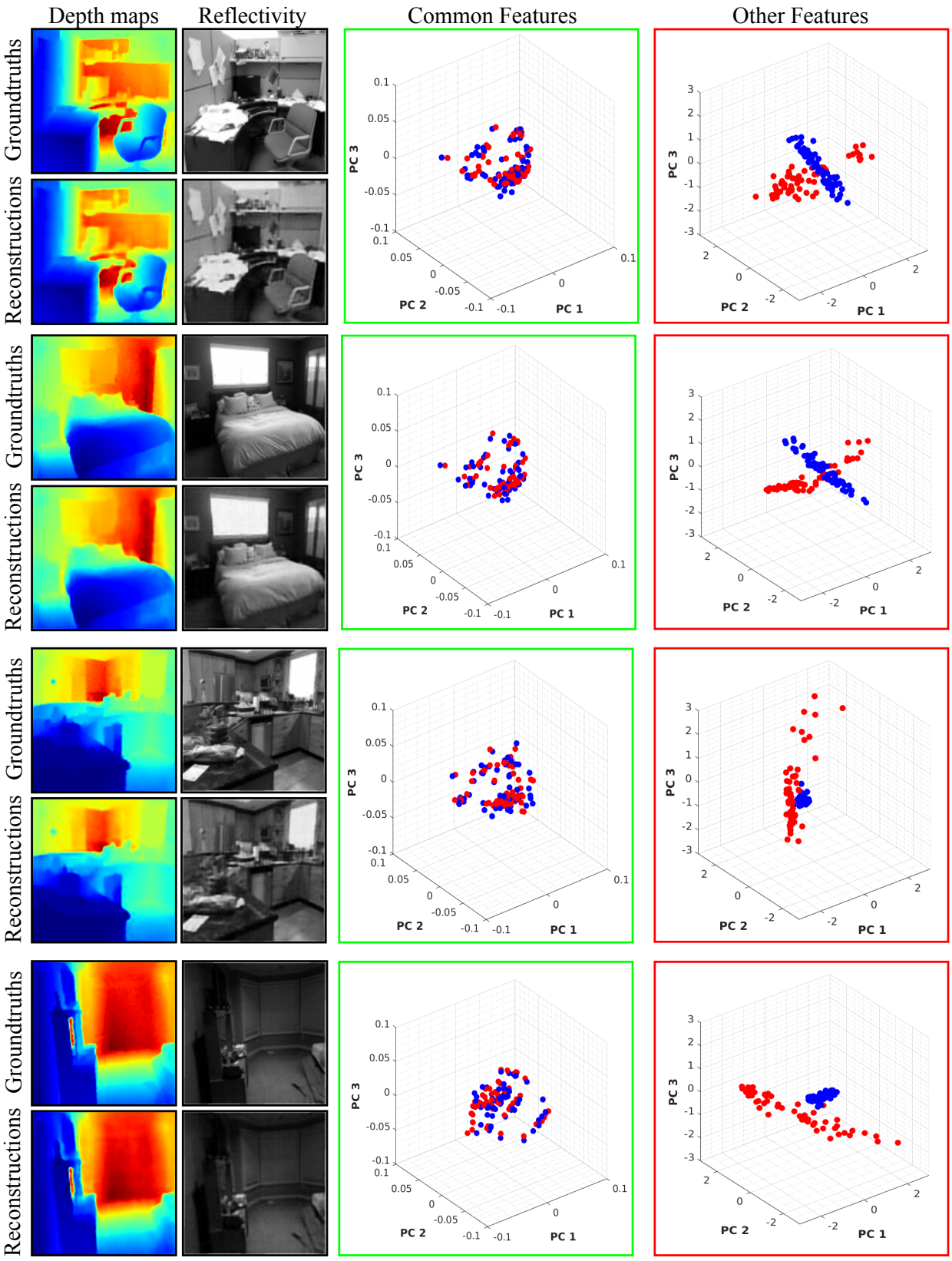

Figure 20. The feature distribution in the low-dimensional space for four scenes shows that the common features are co-located, while the remaining features are dispersed.

References

[1] I. Bar-David. Communication under the poisson regime. *IEEE Transactions on Information Theory*, 15(1):31–37, 1969. 1

[2] Stanley H. Chan, Hashan K. Weerasooriya, Weijian Zhang, Pamela Abshire, Istvan Gyongy, and Robert K. Henderson. Resolution limit of single-photon LiDAR. In *Proceedings of the IEEE/CVF Conference on Computer Vision and Pattern Recognition (CVPR)*, pages 25307–25316, 2024. 1

[3] Prateek Chennuri, Yiheng Chi, Enze Jiang, G. M. Dilshan Godaliyadda, Abhiram Gnanasambandam, Hamid R. Sheikh, Istvan Gyongy, and Stanley H. Chan. Quanta video restoration. In *Computer Vision – ECCV 2024*, pages 152–171, Cham, 2024. Springer Nature Switzerland. 6

[4] Robert K. Henderson, Nick Johnston, Francescopaolo Mattioli Della Rocca, Haochang Chen, David Day-Uei Li, Graham Hungerford, Richard Hirsch, David Mcloskey, Philip Yip, and David J. S. Birch. A 192×128 time correlated SPAD image sensor in 40-nm CMOS technology. *IEEE Journal of Solid-State Circuits*, 54(7):1907–1916, 2019. 5

[5] Ian T. Jolliffe and Jorge Cadima. Principal component analysis: a review and recent developments. *Philosophical Transactions of the Royal Society A: Mathematical, Physical and Engineering Sciences*, 374:20150202, 2016. 6

[6] Ruangrawee Kitichotkul, Joshua Rapp, and Vivek K Goyal. The role of detection times in reflectivity estimation with single-photon lidar. *IEEE Journal of Selected Topics in Quantum Electronics*, 30(1: Single-Photon Technologies and Applications), 2024. 1, 4

[7] Joshua Rapp and Vivek K Goyal. A few photons among many: Unmixing signal and noise for photon-efficient active imaging. *IEEE Transactions on Computational Imaging*, 3 (3):445–459, 2017. 3

[8] Stirling Scholes, German Mora-Martin, Feng Zhu, Istvan Gyongy, Phil Soan, and Jonathan Leach. Fundamental limits to depth imaging with single-photon detector array sensors. *Nature Scientific Reports*, 13:176, 2023. 6

[9] Dongeek Shin, Ahmed Kirmani, Vivek K Goyal, and Jeffrey H. Shapiro. Photon-efficient computational 3-d and reflectivity imaging with single-photon detectors. *IEEE Transactions on Computational Imaging*, 1(2):112–125, 2015. 2, 3

[10] Lihe Yang, Bingyi Kang, Zilong Huang, Zhen Zhao, Xiaogang Xu, Jiashi Feng, and Hengshuang Zhao. Depth anything v2. *arXiv preprint arXiv: 2406.09414*, 2024. 6